
Short-term orbital effects of radiation pressure on the Lunar Reconnaissance Orbiter

Dominik Stiller

B.Sc. student, Faculty of Aerospace Engineering, TU Delft, Netherlands

Abstract

Precision orbit determination for geodetic applications requires force models even for small perturbations. Radiation from the Sun and Moon is a significant source of perturbation in lunar orbits and inadequate modeling of radiation pressure (RP) can lead to large position errors. This paper describes the short-term effect of RP on the Lunar Reconnaissance Orbiter (LRO), which has a position knowledge requirement of 50 m to 100 m in total and below 1 m radially. We compared models of varying complexity to determine the benefits and computational cost of high-accuracy RP modeling. We found that (1) the accelerations differ greatly depending on the Sun position, (2) only a paneled spacecraft model can account properly for changing orientation and geometry of LRO, and (3) a constant-albedo model is sufficient for lunar radiation, which is dominated by the thermal component. A spherical harmonics model for lunar albedo increases computational cost with little gain in the attained accuracy. If RP is neglected, the along-track position errors can be as large as 1100 m and the radial error varies periodically with an amplitude of up to 24 m/s, highlighting the importance of adequate force modeling to meet orbit determination requirements.

Keywords

Radiation pressure, Lunar Reconnaissance Orbiter, precision orbit determination, force modeling

Abbreviations: BRDF bidirectional reflectance distribution function; DLAM-1 Delft Lunar Albedo Model 1; LRO Lunar Reconnaissance Orbiter; RMSE root mean square error; RP radiation pressure; rRMSE relative root mean square error; Tudat TU Delft Astrodynamics Toolbox

1 Introduction

Precision orbit determination is a cornerstone of satellite navigation and spaceborne geodesy. Only if the state, and particularly the position, of the spacecraft are known accurately can the high precision of modern instruments for gravity field recovery or satellite altimetry be exploited fully. Next to tracking data, force models accounting for gravity, solid tides, drag, and other accelerations have the largest role in improving orbit determination. Another important non-conservative force is radiation pressure (RP), which can have magnitudes similar to third-body and irregular gravity field perturbations [1]. RP arises from the exchange of momentum between electromagnetic radiation and the spacecraft. Neglecting or mismodeling RP accelerations can deteriorate position knowledge below acceptable levels.

The Lunar Reconnaissance Orbiter (LRO) was launched in June 2009 to identify safe landing sites, locate resources, and characterize the radiation environment for future human missions to the Moon [2]. To fulfill these objectives, LRO is equipped with instruments to, among other objectives, create high-resolution maps of the lunar topography and gravity field. Accuracies of 50 m to 100 m in the total position and sub-meter accuracy in the radial component are required to take advantage of the instrument resolutions [3, 4], which necessitates force models even for small perturbations. Solar RP “is the largest non-gravitational perturbation affecting

the LRO orbit and inadequate modeling [...] is the primary cause of large prediction errors for LRO, particularly during high-beta angle periods” [5]. The Moon itself is also a significant radiation source since there is no atmosphere and especially the lunar highlands are reflective [6]. The orbit determination error is also highly dependent on the modeling of how RP translates to accelerations; particularly during full-Sun periods, a model accounting for LRO’s geometry and the real orientation of the solar array and high gain antenna outperforms a simple spherical model [7].

This paper describes the short-term effects of RP on LRO’s orbit and the sensitivities of these effects to models of varying complexity. Other authors have already described their orbit determination approaches for LRO [5, 7–13], but none compared RP modeling choices and their implications. Vielberg and Kusche investigated the effect of different models for Earth [14], where a plethora of observations are available and the radiation environment differs greatly from the Moon. Therefore, their results do not apply to orbits around the Moon. Our paper alleviates this lack of guidance for lunar orbits by elucidating the choice of force models for orbit determination both in terms of accuracy and computational performance. The results relate to short-term effects over 2.5 days, which is a typical arc used in orbit determination. Long-term effects, which may cancel or compound over the span of months, are not considered here.

The TU Delft Astrodynamics Toolbox (Tudat) was used for all orbital simulations and the models presented here were integrated into the software, which is freely available at <https://docs.tudat.space/>.

2 Radiation pressure modeling

RP modeling requires the cooperation of models for the radiation sources and the spacecraft. This section describes a collection of compatible models, starting with a physical description of RP and reflectance, then building models of increasing complexity on top of that.

2.1 Mechanics of radiation pressure

RP results from the momentum transfer between electromagnetic radiation and a surface. A spacecraft may receive such radiation from the Sun but also from other celestial bodies: planets and moons emit albedo radiation through the reflection of sunlight and thermal radiation depending on surface temperature. The RP exerts a force on the spacecraft governed by surface properties such as area, reflectivity, and absorptivity. The resulting acceleration is the result of a complex interplay of the bodies emitting radiation (the “sources”) and the spacecraft receiving the radiation (the “target”).

Radiation can be characterized by the radiant flux density, which commonly has units of W/m^2 . Radiosity is the *emitted and reflected* radiant flux density of an opaque surface. The irradiance E is the *incident* radiant flux density on a surface and provides a convenient way to decouple source and target models: the irradiance and the direction of incidence are sufficient to determine the target acceleration, independent of the actual source. We can combine this information into a vector quantity which we call directional irradiance $\mathbf{E} = E\hat{\mathbf{r}}_{t/s}$, where $\hat{\mathbf{r}}_{t/s}$ is the unit vector in the source-to-target direction. One or more directional irradiances, which can be thought of as light rays, are the output of a source model and are used as input to the target model. The RP exerted on an irradiated surface is proportional to $1/c$, where $c = 299\,792\,458 \text{ m/s}$ is the speed of light. Given the magnitude of c , RP is usually small (around $4.5 \times 10^{-6} \text{ N/m}^2$ for solar radiation at Earth, where $E = 1361 \text{ W/m}^2$ [15]).

Electromagnetic radiation is often composed not just of a single wavelength but rather a range of wavelengths. The distribution can be described by the spectral irradiance in units of $\text{W}/(\text{m}^2 \text{ Hz})$. Since surface properties are often wavelength-dependent, the target model would also have to be aware of the distribution. However, the surface properties as a function of wavelength are often not known, which is also the case for LRO. Therefore, we assume the irradiance from source models to be integrated over the whole spectrum and the surface properties of the target model to be valid for all wavelengths.

2.2 Reflectance distribution

Describing the reflectance of a surface is key to RP modeling. Both the way a source reflects sunlight and the direction a target is accelerated depend on the angular distribution of reflectance.

General reflectance distribution In general, reflectance comprises a diffuse (scattered in many directions) and a specular (mirror-like) component. The remaining energy is absorbed by the surface. The reflectance varies with surface normal \mathbf{N} , incoming radiation direction \mathbf{L} , and observer direction \mathbf{V} . This geometry is shown in Figure 1. A bidirectional reflectance distribution function (BRDF)

describes the fraction of irradiance reflected toward the observer per steradian, i.e. [16]

$$f_r(\theta_i, \phi_i, \theta_r, \phi_r) = \frac{dL_r(\theta_r, \phi_r)}{dE_j(\theta_i, \phi_i)}, \quad (1)$$

where dL_r is the reflected radiance (the directional counterpart to radiosity, typically in $\text{W}/(\text{m}^2 \text{ sr})$) and dE_j is the received irradiance.

The planetary surface BRDF directly leads to the albedo irradiance received by a target if the solar irradiance at the planet’s surface and the solid angle subtended by the target are known.

The target surface BRDF gives the direction in which the target is accelerated through integration over all directions \mathbf{V} in which radiation is reflected. The unitless reaction vector, which includes both the direction and magnitude based on absorbed, specularly reflected, and diffusely reflected fractions, is therefore [16]

$$\mathbf{R} = - \left[\mathbf{L} + \int_0^{2\pi} \int_0^{\pi/2} f_r \cos \theta_r \mathbf{V} d\theta_r d\phi_r \right]. \quad (2)$$

This vector encapsulates the mechanics of momentum transfer. The reaction is minimal for pure absorption ($f_r = 0$) and maximal (double the minimum) for pure specular reflection in the incidence direction.

Specular–diffuse reflectance distribution A simplified BRDF is usually more practical for RP modeling: the reflectance is assumed to be a mix of an ideal Lambertian diffuse component and a purely mirror-like specular component. Such a BRDF is given by [16]

$$f_r = C_d \frac{1}{\pi} + C_s \frac{\delta(\mathbf{V} - \mathbf{M})}{\cos \theta_i} \quad (3)$$

where C_d and C_s are the diffuse and specular reflectivity coefficients. Together with the absorption coefficient C_a , energy is conserved when $C_a + C_d + C_s = 1$. The vector $\mathbf{M} = 2 \cos \theta_i \mathbf{N} - \mathbf{L}$ is the direction of \mathbf{L} ’s mirror-like reflection, which only contributes if $\mathbf{V} = \mathbf{M}$.

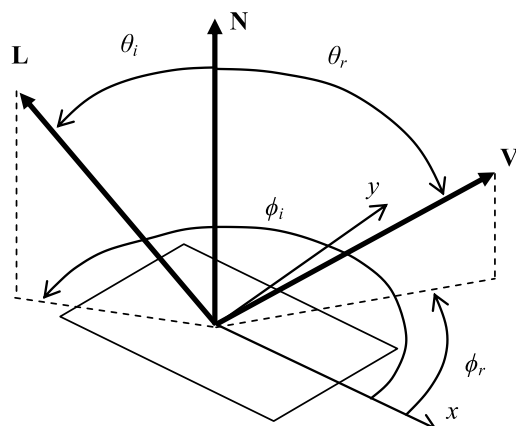


Figure 1. Geometry of a BRDF for a surface with normal \mathbf{N} , incoming direction \mathbf{L} , and observer direction \mathbf{V} . The viewing angle θ_r is between \mathbf{N} and \mathbf{V} . The phase angle (not labeled) is between \mathbf{L} and \mathbf{V} . Adapted from [16].

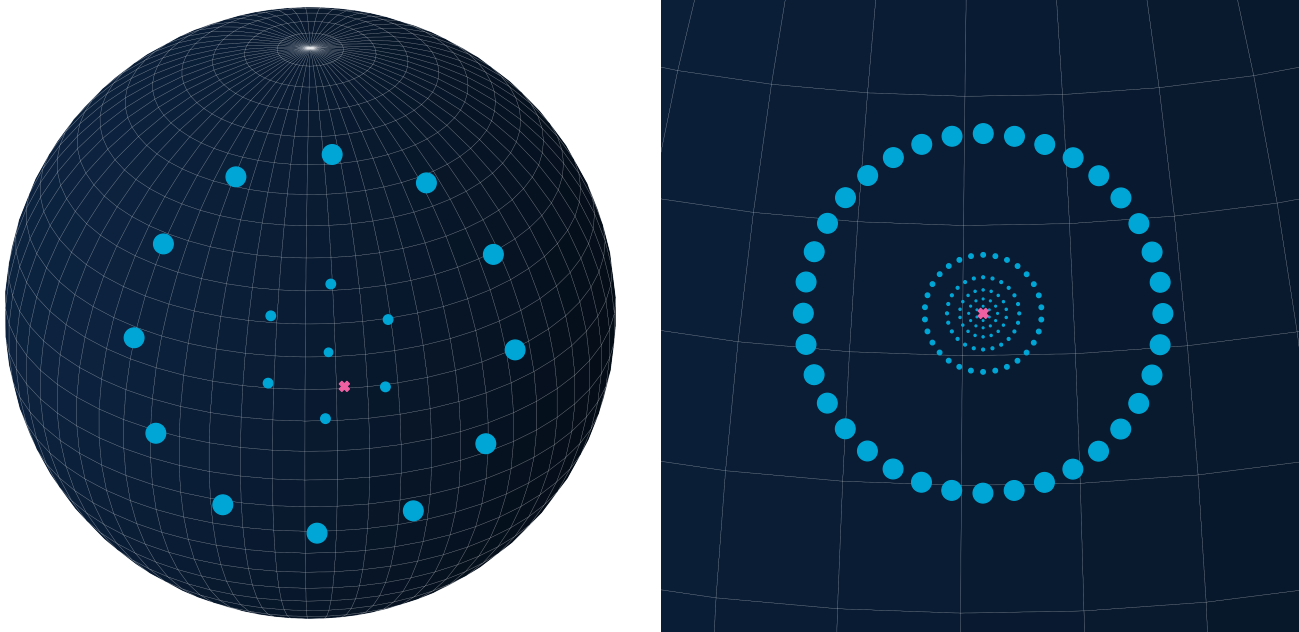


Figure 2. Panels generated with Knocke's algorithm for the Moon, which has a mean radius of 1737 km. The spacecraft (✖) sees a spherical cap (—), which contains rings of panels and is larger at higher altitudes h . Panel centers (●) are scaled proportional to the panel area. The panels have equal projected, attenuated areas and are therefore concentrated around the subsatellite point. The scenario in **b** corresponds to LRO's orbit and the paneling used in this paper.

the edge of the visible cap. This pattern is a result of the equal projected, attenuated areas.

Paneled sources: Radiosity models The emitted and reflected fluxes of a panel are described by a radiosity model. The irradiance at the target position can then be derived from the panel radiosity. Both radiosity and irradiance commonly have units of W/m^2 . Each panel can have one or more radiosity models, usually one for albedo radiation and one for thermal radiation. We present three such models.

The albedo radiosity model accounts for diffuse Lambertian reflection of solar radiation. It implements the specular-diffuse BRDF from Equation (3) with $C_s = 0$ and the albedo value $C_d = a$ at the panel center. The albedo radiosity of a panel is [22]

$$J_{\text{albedo}} = a (\cos \theta_i)_+ E_s, \quad (9)$$

where E_s is the incoming solar irradiance at the panel (e.g., as found from Equation (6)) and the solar incidence angle θ_i is defined in Figure 1. The operator $(\cdot)_+$ restricts the input to positive values or zero otherwise. This ensures that no radiation is reflected from the backside.

The delayed thermal radiosity model assumes that absorbed radiation is emitted independently of incident solar radiation and the radiosity is thus not a function of θ_i . The only spatial variations arise from emissivity differences. The emissivity e of a surface is the ratio of the actual radiosity to the ideal black body radiosity. The delay arises from the planet's large thermal inertia. The delayed thermal radiosity of a panel is [22]

$$J_{\text{thermal}} = e \frac{E_s}{4}, \quad (10)$$

where e is the emissivity of the panel, evaluated at its center. The factor $1/4$ is the ratio of the absorbing area (a circle) to emitting area (a sphere). The albedo and delayed thermal model were originally used by Knocke *et al.* for Earth emissions [22].

The angle-based thermal radiosity model is more appropriate than the delayed model if the surface experience significant diurnal cooling and heating. The surface temperature is modeled as a function of the solar incidence angle θ_i and related to the radiosity through the Stefan-Boltzmann law. The surface temperature is interpolated between the minimum and maximum temperatures, T_{\min} and T_{\max} as

$$T = \max \left(T_{\max} (\cos \theta_i)_+^{1/4}, T_{\min} \right). \quad (11)$$

These temperatures typically correspond to the nighttime temperature and the temperature at the subsolar point. The angle-based thermal radiosity of a panel is then [27]

$$J_{\text{thermal}} = e \sigma T^4, \quad (12)$$

where T is the surface temperature from Equation (11) at the panel center and $\sigma = 5.670 \times 10^{-8} \text{ W}/(\text{m}^2 \text{ K}^4)$ is the Stefan-Boltzmann constant. On the dayside, the radiosity is proportional to $T_{\max}^4 \cos \theta_i$. The maximum radiosity of $e \sigma T_{\max}^4$ is usually larger than the near-constant $e E_s / 4$ from Equation (10), but quickly decreases as the panel moves away from the subsolar point (where $\theta_i = 0^\circ$). On the nightside, the thermal radiosity reduces to $e \sigma T_{\min}^4$.

The albedo and thermal radiosity models depend on the distribution of a and e over the planetary surface. The values may be assumed constant but generally vary with longitude, latitude, and time. Particularly for Earth, seasons and weather

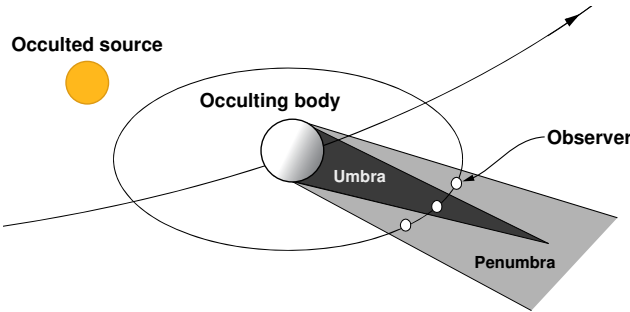


Figure 3. Conical occultation model for spherical sources and occulting bodies. The observer is partially illuminated in the penumbra but fully shadowed in the umbra. Adapted from [33].

observer receive the full radiation ($\nu = 1$). In the case of a lunar eclipse, Earth occults the Sun and casts a shadow onto the Moon such that there is no lunar albedo radiation. On the nightside of a planet, the planet itself occults the Sun.

With the models described in Sections 2.3 and 2.4, the shadow function needs to be considered for radiation from a point source, both when directly incident on the target and when used as solar radiation for albedo radiosity. The extent of the source and occulting bodies needs to be known for shadow function calculations, even in the case of point sources. A derivation of the conical model for ν is presented by Montenbruck and Gill [1].

The conical model can only account for one occulting body. In the case of multiple occulting bodies, shadows might overlap and the product of their shadow functions would underestimate the actual received fraction. Knowledge of the shadow intersection would be required to avoid this. Zhang *et al.* derived a model for two occulting bodies [34]. However, only single occultations are considered in this paper.

More involved shadow models exist that improve the prediction of the penumbra passage. These models can consider planetary oblateness and atmospheric effects like absorption, scattering, and refraction [35]. Other models can account for topography by combining a paneled Sun model with a topography map [9]. These modifications usually prolong the penumbra duration.

Point-to-point visibility For source panels represented by their center point, the shadow function becomes binary: either there is a line of sight between the panel center and the target or there is not. Such point-to-point visibility with a spherical occulting body is easily modeled geometrically. A derivation is given by Vallado and Wertz [33]. Multiple occultations are supported in this occultation model by the logical conjunction of the individual visibilities.

3 Radiation pressure modeling for LRO

After describing RP modeling in general, we now present models that are relevant to LRO. This includes the source models for lunar radiation and the target models. We also elaborate LRO's orbit geometry and the simulation setup.

3.1 Lunar albedo radiation

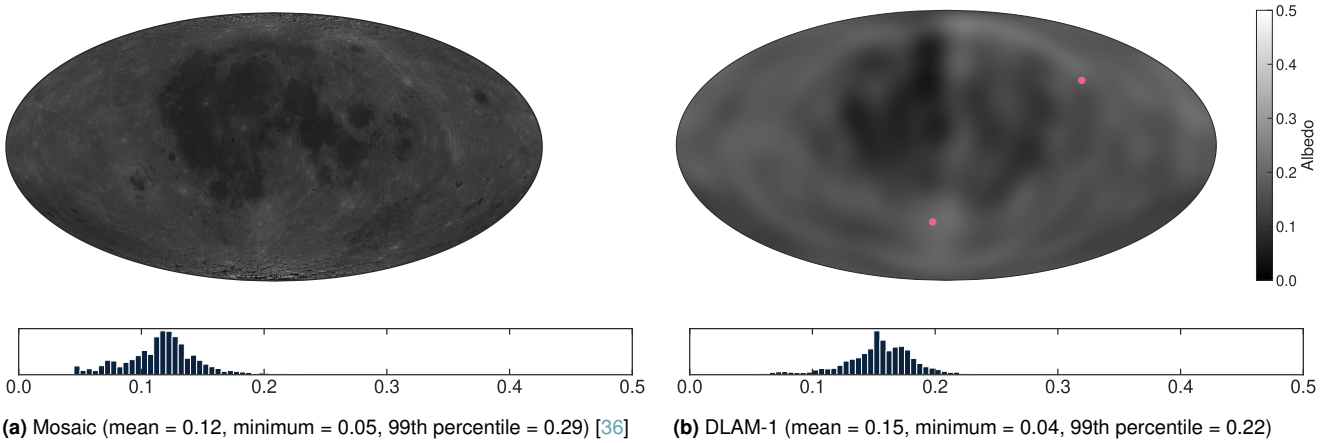
The Moon is a major source of radiation in LRO's orbit, with lunar irradiance magnitudes approaching half of the Sun's. Therefore, albedo and thermal radiation due to the

Moon are modeled. While the lunar albedo is only 40 % of Earth's albedo [28], albedo radiation due to the Moon is still substantial, particularly over the subsolar point [6]. Lunar albedo varies significantly with geology: the highlands (mean $a = 0.16$, maximum $a = 0.25$) are much more reflective than the maria (mean $a = 0.07$, minimum $a = 0.05$) due to their respective regolith composition [37–39]. The mosaic of calibrated albedo imagery from Clementine in Figure 4a clearly shows the differences between highlands and maria. The mean of 0.12 agrees with other literature [37], and most of the lunar surface has an albedo below 0.20. Higher values are only found at the poles, where the imagery represents topographic shading rather than actual albedo [40]. Note that the mosaic is for the albedo of light at 750 nm wavelength, which is slightly longer than the average solar wavelength. Even though solar radiation has the most energy within the 300 nm to 2400 nm band, the spectrum peaks at around 470 nm [41]. Lunar reflectivity increases with increasing wavelength [42].

Floberghagen *et al.*'s 15×15 spherical harmonics expansion called Delft Lunar Albedo Model 1 (DLAM-1) [6] is often used to represent this spatial albedo variability in lunar RP models. DLAM-1 was fitted from Clementine imagery and was designed to work with Knocke's albedo model for dynamic paneling (Equation (9)). Due to the nature of spherical harmonics, the model cannot resolve features smaller than 12° (360 km at the equator). The expansion is shown in Figure 4b, along with direct imagery from Clementine. DLAM-1 was also derived from 750 nm imagery, but we scale the original values by 1/1.3 to account for the reduced reflectivity at the average solar wavelength. This factor was proposed by Vasavada *et al.* [37]. Even with the correction, the mean albedo of the expansion of 0.15 is still 25 % above the commonly accepted mean of 0.12. This is possibly due to a different calibration of the imagery that DLAM-1 is based on compared to the mosaic from Figure 4a. In fact, Clementine is known to overestimate albedo due to bad calibration [42]. Apart from the difference in magnitude, the patterns agree reasonably well: Maria and highlands are distinct, and large bright features like the ray system around the Tycho and Giordano Bruno craters can be recognized (marked in Figure 4b).

Despite the shortcomings of DLAM-1, spherical harmonics are convenient: they are smooth and do not require interpolation like a gridded map. They can easily be truncated to trade detail for computational efficiency. Therefore, we used DLAM-1 in this paper but consider that the magnitude may be overestimated by 25 % during the analysis of results. We also compare results for the location-dependent DLAM-1 with those for a constant value, which should be more computationally efficient. As a single representative albedo, we choose the mean of 0.15 instead of 0.12 to facilitate comparison. Note that the spatial variability described above suggests that a single albedo value cannot accurately represent lunar reflectivity.

Albedo radiation assumes ideal, diffuse Lambertian reflectance, which decreases with the cosine of the viewing angle. This assumption is especially appropriate for Earth, for which purely specular radiosity only amounts to 10 % of the purely diffuse radiosity [22]. However, this is not the case for the Moon: the opposition effect increases the



(a) Mosaic (mean = 0.12, minimum = 0.05, 99th percentile = 0.29) [36]

(b) DLAM-1 (mean = 0.15, minimum = 0.04, 99th percentile = 0.22)

Figure 4. Lunar albedo distribution from Clementine. Both the mosaic and DLAM-1 are based on 750 nm reflectivity, but DLAM-1 has been corrected to the average solar wavelength. Large bright features like the Tycho and Giordano Bruno craters (●) can be registered. Note that the maximum of the albedo scale here is 0.5 instead of 1.0 to increase contrast; in reality, the Moon appears half as bright.

reflectance at low phase angles (when the source is behind the observer, see Figure 3) much more than would be expected from a cosine law. In fact, the brightness increases more than 40 % between phase angles of 4° and 0° [43]. This is primarily caused by shadow hiding. To account for the non-diffuse reflectance of the lunar surface, the Hapke BRDF was developed [44]. This BRDF is an empirical relation based on nine parameters that control, among other phenomena, the strength and directionality of the opposition effect. Near-global maps for these parameters have been fitted from LRO observations and could be used for a radiosity model [39]. For RP acceleration modeling, the opposition effect is only of concern when the target is above the subsolar point; the Sun has to be in the orbital plane for this. For LRO, this only occurs for a few days twice a year, and even then only for a small fraction of the orbit. Therefore, we neglect the opposition effect in this study.

3.2 Lunar thermal radiation

Lunar surface temperatures and the associated thermal radiation undergoes a significant diurnal cycle. Daytime and nighttime temperatures can differ by up to 290 K. The surface heats rapidly after sunrise, cools at about the same rate after local noon, then slower during the night [37]. There are small seasonal changes, with noon temperatures differing by 6 K between lunar aphelion and perihelion [23]. The large diurnal variability makes Knocke's delayed thermal model (Equation (10)), which gives constant radiosity throughout the day, unsuitable for the Moon.

Diurnal variability is represented well by the angle-based thermal model (Equation (12)). We parametrize the model with the equatorial temperatures just before sunrise ($T_{\min} = 95$ K) and at local noon ($T_{\max} = 385$ K). The model transitions to the nighttime temperature when the incidence angle $\theta_i \geq 89.8^\circ$. The temperatures span a slightly larger range than Lemoine *et al.* ($T_{\min} = 100$ K, $T_{\max} = 375$ K), who initially proposed the angle-based model. However, they agree with those used by Park *et al.* [45]. Note that Park *et al.*'s model is identical to ours except for a factor 1/4 in the radiosity, which is incorrect.

While the albedo varies with location (see Section 3.1), the emissivity and other thermophysical properties are remarkably uniform [38]. This means that constant emissivity is a fair assumption. We used a value of $e = 0.95$, which is the broadband daytime emissivity, although it decreases to 0.90 during the night [46]. However, we assume the constant daytime emissivity at all times.

The thermal surface radiosity J_{thermal} from the angle-based model with the aforementioned parameters is shown in Figure 5. The radiosity decreases with the cosine of the incidence angle and approaches negligible emissions of 6 W/m^2 at nighttime. The maximum radiosity, which occurs below the subsolar point (i.e., at local noon), is 1246 W/m^2 . This peak value agrees with those used to design LRO's thermal control subsystem [2]. The only effect that is not captured is the slow cooling by about 25 K between sunset and sunrise [37], which introduces a slight asymmetry; constant pre-sunrise temperatures are used throughout the night. We also do not model seasonal variations of surface temperature.

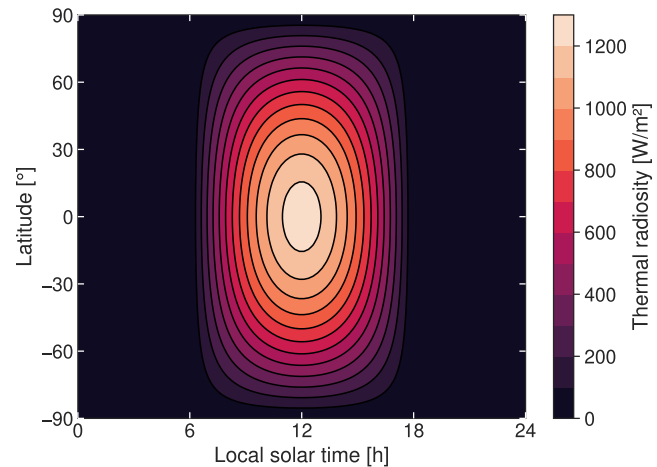


Figure 5. Map of lunar thermal emissions from the angle-based model (Equation (12)). The emissivity is 0.95 and surface temperatures range between 95 K and 385 K, depending on the subsolar angle.

Table 3. Common setup for all simulations. Gravity and radiation pressure are the only force models.

Planetary bodies	
Planetary ephemerides	DE 421 [50]
Moon ellipsoid	Sphere of radius 1737.4 km [51] (no flattening)
Moon reference frame	Mean Earth/Polar Axis [52]
Force models	
Moon gravity	GRGM1200L [53] (truncated to 100×100)
Earth + Sun gravity	Central
Solar radiation	Isotropic point source ($L = 3.828 \times 10^{26}$ W [19]) Occulted by Moon
Lunar radiation	Paneled source with 6 rings of 6, 12, 18, 24, 30, and 36 panels Albedo: Constant ($a = 0.150$) or DLAM-1
RP target	Thermal: Angle-based ($e = 0.95$, $T_{\min} = 95$ K, $T_{\max} = 385$ K) Cannonball ($A_c = 14 \text{ m}^2$, $C_r = 1.0$) or Paneled (see Table 1) Paneled model with or without instantaneous reradiation Mass: 1087.0 kg (end of science mission) Orientation: LRO_SC_BUS frame from SPICE CK
Simulation settings	
Software	TU Delft Astrodynamics Toolbox (Tudat) 2.12.1.dev19
Propagation frame	ECLIPJ2000
Propagation method	Cowell
Integration method	Runge–Kutta–Fehlberg 7(8)
Step size	5 s (fixed)
Arc length	2.5 days (31.9 revolutions)
Initial state	Cartesian state from SPICE SPK (lrorg_*)

and is useful to compare differences across orders of magnitude.

While the simulation evaluates accelerations in a global frame, the effect of accelerations on the orbit is best analyzed in a spacecraft-fixed coordinate system that is aligned with the orbital track. The RSW coordinate system is one such system, defined by the unit vectors [33]

$$\mathbf{R} = \frac{\mathbf{r}}{\|\mathbf{r}\|}, \quad \mathbf{W} = \frac{\mathbf{r} \times \mathbf{v}}{\|\mathbf{r} \times \mathbf{v}\|}, \quad \text{and} \quad \mathbf{S} = \mathbf{W} \times \mathbf{R}. \quad (18)$$

The radial component \mathbf{R} is aligned with the planetocentric position vector \mathbf{r} . The cross-track component \mathbf{W} is aligned with the angular momentum vector, or orbit plane normal, involving the linear velocity \mathbf{v} . The along-track component \mathbf{S} completes the right-handed coordinate system. Note that \mathbf{S} is generally not perfectly aligned with the velocity vector, only for circular orbits.

4.1 Instantaneous reradiation

First, we investigated the effect of instantaneous reradiation for the paneled target model. This increases the acceleration proportional to each panel's C_a , normal to the panel (cf. Equation (5)).

Figure 10 shows the absolute and relative differences between accelerations without and with instantaneous reradiation. In absolute terms, the radial and along-track components are impacted most for the September arc, while the along-track and cross-track components experience the largest increase for the June arc (for both arcs, up to about $1.9 \times 10^{-8} \text{ m/s}^2$ RMSE). The relative differences are more uniform (around 40 % rRMSE), but the along-track

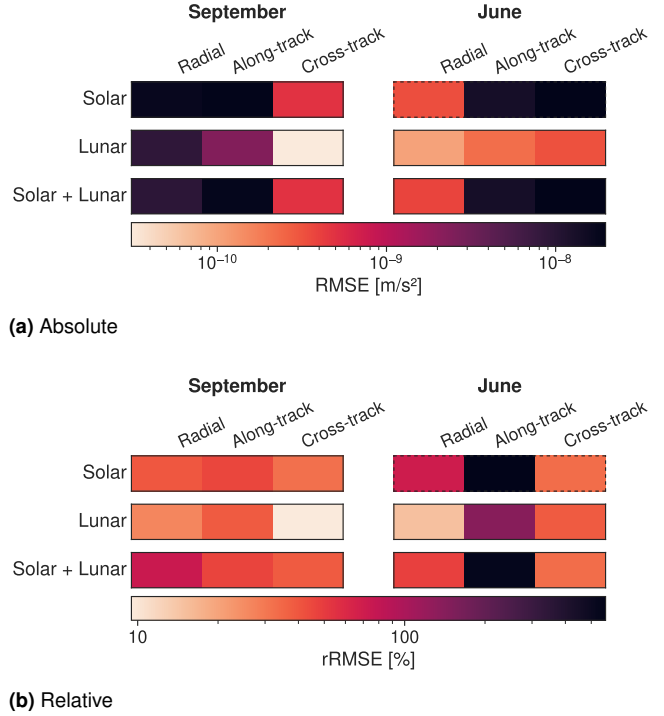


Figure 9. RMS differences of RP accelerations over one orbit with and without instantaneous reradiation. The dashed boxes correspond to Figure 10.

components of lunar and solar radiation in the June arc increase by 140 % and 570 % rRMSE, respectively. In most cases, only the magnitude of accelerations changes but not the pattern.

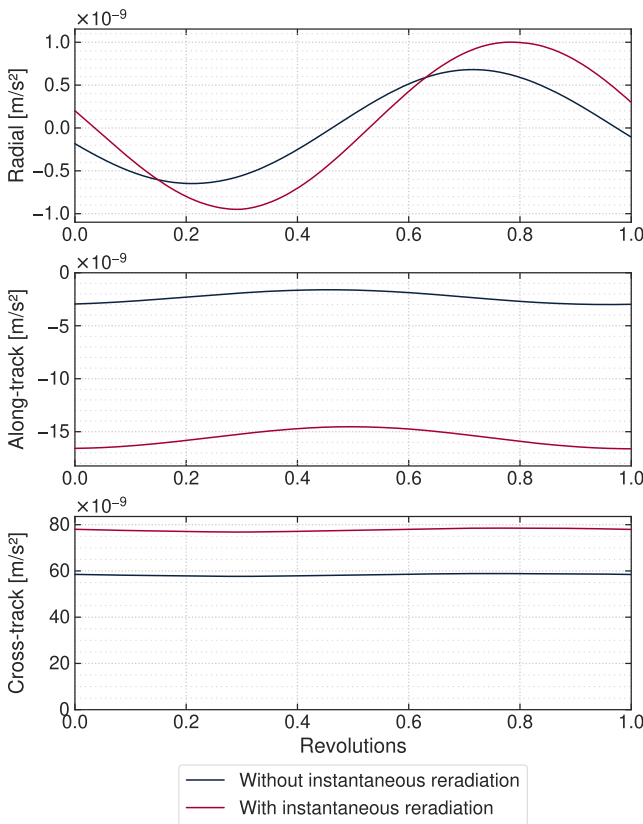


Figure 10. Accelerations due to solar radiation without and with instantaneous reradiation over one orbit for the June arc. There is a phase shift in the radial component and the along-track component increased by 570 % RMSE. Lunar contributions and the September arc are not significantly affected in shape.

Figure 10 shows the solar radiation of the June arc without and with instantaneous reradiation, the only of our simulations for which the pattern changed significantly. The phase of the radial acceleration is shifted by about 10 % of the orbital period, which is not the case for the other two components or the acceleration due to lunar radiation. This arc also had the largest relative change in along-track acceleration as described above (highlighted in Figure 9). This change manifests as a constant offset of about $-13 \times 10^{-9} \text{ m/s}^2$.

The large changes seen in some cases are mostly due to the +SA panel, which is highly absorptive ($C_a = 0.90$) and large ($A = 11.00 \text{ m}^2$). For the June arc, the solar array is angled at 45° with equal components in the cross-track and along-track directions. The Sun is on the same side as the solar array in the cross-track direction. Without instantaneous reradiation, no panel has a significant contribution to the along-track acceleration, so it is quite small at around $2 \times 10^{-9} \text{ m/s}^2$. With instantaneous reradiation, each panel, and especially the solar array, exerts an acceleration parallel to its normal, which leads to the along-track increase witnessed for the June arc.

We applied instantaneous reradiation for all of the following simulations since no reradiation due to spacecraft panels is physically unrealistic and the differences in magnitude are significant when instantaneous reradiation is added. More sophisticated thermal models involving conduction and internal heat generation would likely produce more accurate results.

4.2 Accelerations

The most direct effect of RP is visible in the accelerations. Therefore, we compare the RP accelerations

- for the September and June arcs,
- due to solar and lunar (albedo + thermal) radiation,
- for the constant and DLAM-1 albedo distributions,
- for the cannonball and paneled targets.

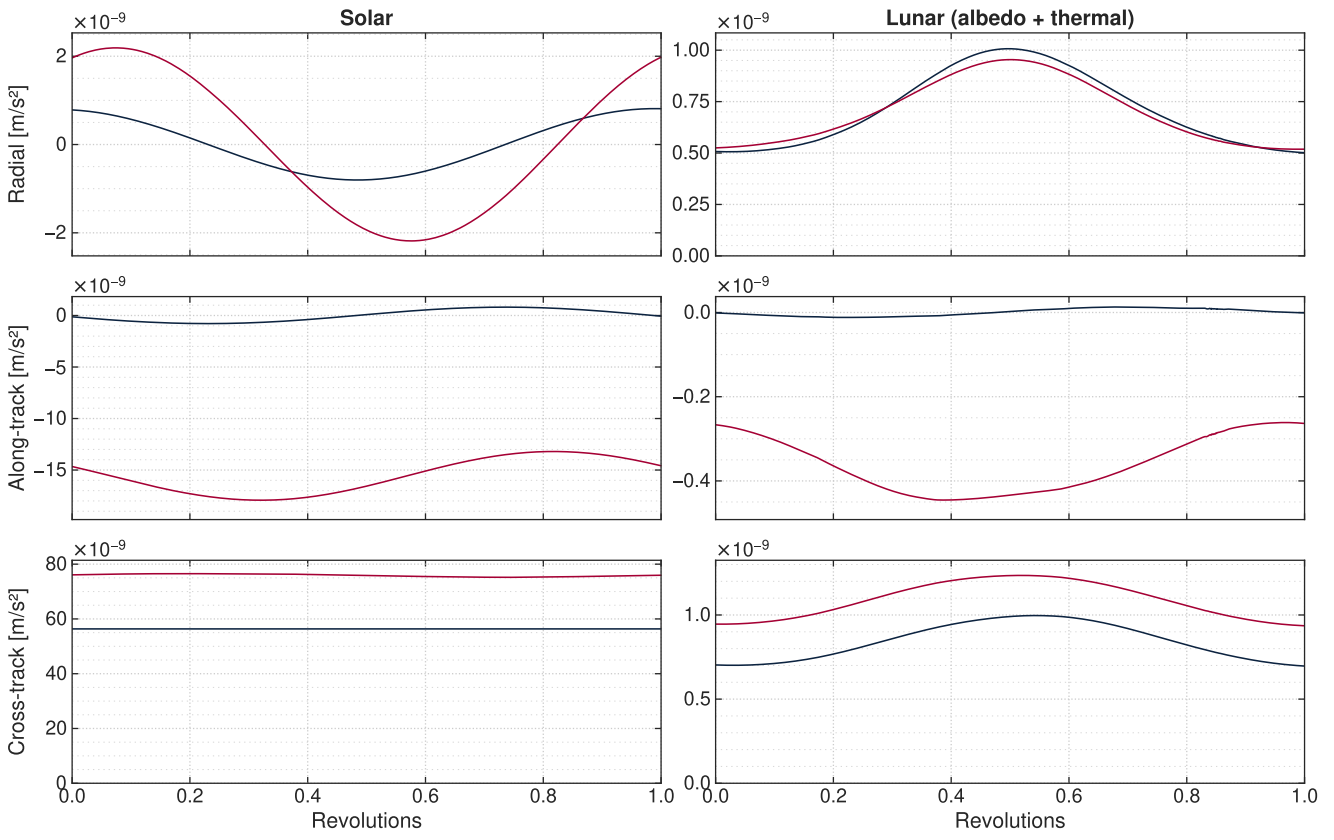
In total, we ran 46 simulations. All accelerations are given in 10^{-9} m/s^2 . Regarding the cannonball and paneled target models, note that their comparative magnitudes are less important since the choice of cannonball parameters is somewhat arbitrary. Instead, we compared their behaviors and how they relate to model assumptions (e.g., symmetry for the cannonball, tracking for the paneled target).

Solar and lunar radiation Both solar and lunar radiation are significant but their accelerations may amplify or cancel each other. To compare them, we used a constant albedo model in addition to the thermal model. The accelerations over one orbit are shown in Figure 11. Note that secular variations in orbit geometry can change the magnitude of acceleration components across orbits even within one 2.5-day arc but are not shown here.

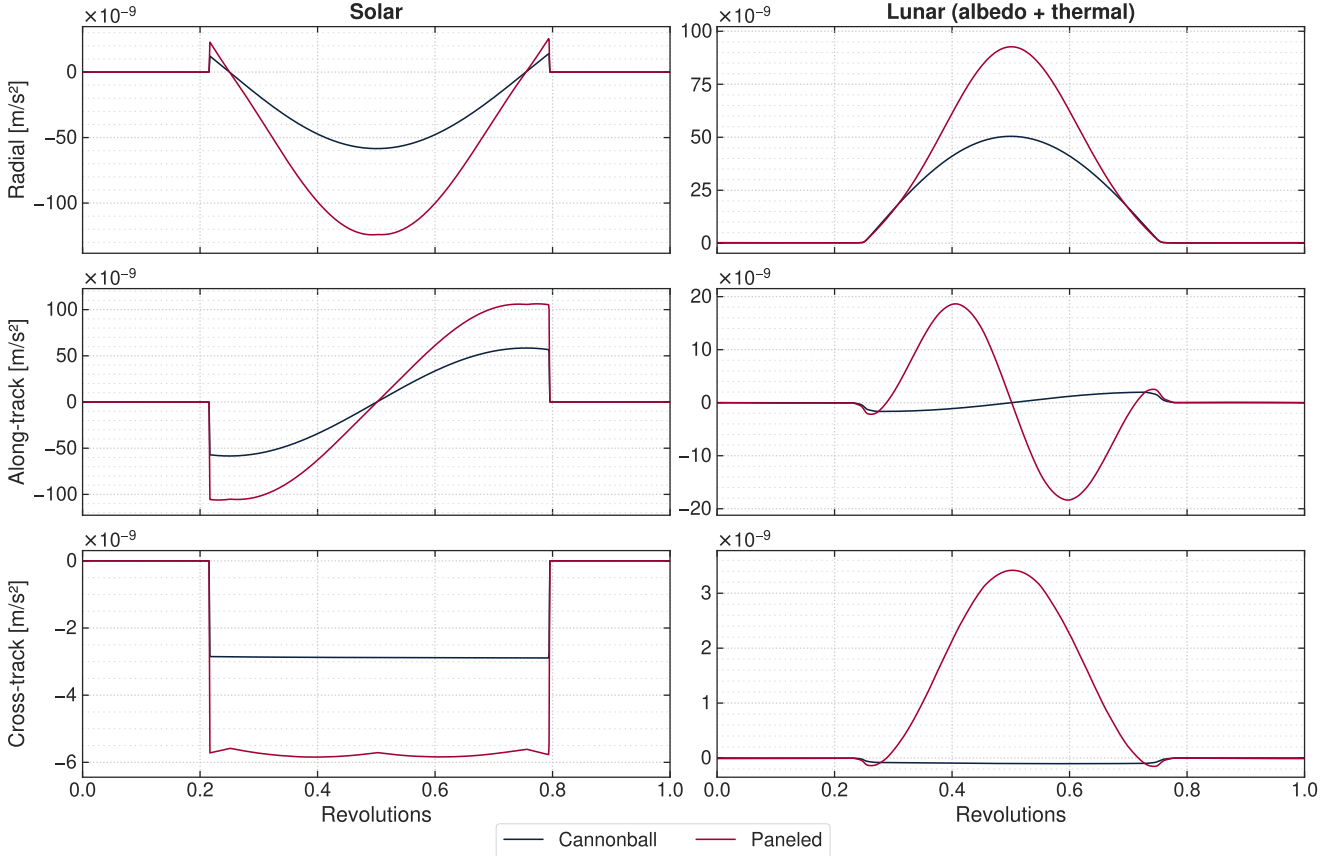
For the June arc (Figure 11a), the spacecraft is in permanent sunlight and the orbit plane normal points toward the Sun because $\beta \approx 90^\circ$. This leads to extremely large, constant cross-track solar accelerations. The paneled model also has along-track solar accelerations due to the solar array as explained in Section 4.1. Interestingly, the radial solar accelerations show the same phase shift between the cannonball and paneled targets as observed without instantaneous reradiation (Section 4.1). This suggests that symmetry, or the lack thereof, is the cause of the phase shift. The magnitude of the total solar acceleration does not change much throughout the year since it is only dependent on the Moon–Sun distance, which is relatively constant at 1 au (see Table 2).

The lunar accelerations during the June arc are generally small (less than 2 % of solar) because LRO never passes over well-illuminated regions; half of the lunar source panels that are visible by LRO are on the nightside and therefore rarely contribute. The sinusoidal variations in lunar radiation pressure are mainly caused by the fact that β is not exactly 90° and LRO's angle to the subsolar point therefore varies by 2° . Periodic variations in altitude due to the eccentricity itself have a minimal effect since higher altitudes mean larger distances but also a larger visible area of the lunar surface, which roughly cancels. Secular variations in lunar accelerations (not shown) exist and are due to the evolution of eccentricity over the 2.5 days caused by the non-uniform lunar gravity field [2]. The eccentricity ranges from 0.005 to 0.008, which leads to periselene altitudes between 37 km and 41 km. Such changes in eccentricity lead to larger amplitudes but no mean shift.

For the September arc (Figure 11b), the Sun is occulted for 42 % of the orbit since $\beta \approx 0^\circ$. The effect of these occultations is evident in solar and lunar radiation, both of which vanish on the nightside. The accelerations are mostly in the radial and along-track directions. This is most clearly explained by the solar accelerations: At 0.2, LRO



(a) June



(b) September

Figure 11. Accelerations due to solar and lunar radiation over one orbit. The cannonball and paneled targets differ both in magnitude and pattern of accelerations. Note the different scales of each subplot.

crosses the terminator above the pole and is moving straight toward the Sun; the along-track component is then maximal and negative since the Sun opposes the spacecraft's motion. Continuing the orbit, LRO passes above the subsolar point at 0.5, leading to a maximal and negative radial component while the along-track component has vanished. Further toward the other pole, LRO passes into the night at 0.8, where the along-track component accelerates the spacecraft into the direction of motion. During this whole time, the cross-track component is slightly negative because β is slightly negative but not zero. If β were slightly positive, the cross-track component would be similar but with the sign flipped. In addition to periodic changes, there is a secular change in solar accelerations (not shown) since the already slightly negative β continues to decrease: over the 2.5-day arc, the mean of the along-track and cross-track components increase twofold and threefold, respectively. This trend continues until the cross-track component dominates for high β , as seen for the June arc.

The lunar accelerations during the September arc are much larger than during the June arc because LRO passes right over the subsolar point, which reflects much sunlight and has high thermal emissions. Indeed, the lunar irradiance (up to 1831 W/m^2) is larger than the solar irradiance (up to 1362 W/m^2) above the subsolar point. Still, the lunar acceleration magnitude is 14 % smaller than the solar acceleration magnitude since lunar panels are distributed azimuthally around the nadir and thus partially cancel while all solar rays are parallel. Another feature of lunar accelerations is the sign opposite to solar accelerations: when passing over the subsolar point, the radial components of solar and lunar accelerations roughly cancel. A similar effect can be seen in the along-track and cross-track components for a paneled target, although the lunar radiation needs some time to build up: The along-track component peaks at a subsolar angle of 33° , the cross-track component above the subsolar point. The cross-track component increases secularly over the 2.5-day arc, similarly to solar radiation.

Comparing the accelerations of cannonball and paneled targets for both arcs, it is clear that a single C_r cannot capture the complex and changing spacecraft geometry. While the solar accelerations for the September arc are just off by about a constant factor, this is not the case for the June arc or any of the lunar accelerations. In fact, the sign may even be different, particularly for lunar along-track and cross-track accelerations in September. This is likely caused by the solar array tracking the Sun. On smaller scales, the effect of target panels of different sizes and reflective properties becoming illuminated as LRO revolves around the Moon can be seen in the kinks of the solar cross-track accelerations of the September arc.

All accelerations are inversely proportional to the spacecraft's mass. While we chose the end-of-mission mass for all simulations, the begin-of-mission mass is 17 % higher and all accelerations are thus 17 % lower (see Section 3.4). This only changes magnitudes, not patterns.

Lunar albedo and thermal radiation In the previous subsection, lunar radiation was considered as the sum of albedo and thermal radiation. In this subsection, we look at the separate contributions and the differences between albedo

distributions. The accelerations on a paneled target are shown in Figure 12.

For both arcs and all components, thermal radiation is far larger than albedo radiation (up to sixfold). This is even though the albedo is likely overestimated by 25 % as described in Section 3.1. In terms of behavior, the thermal radiation and constant albedo radiation are very similar: smooth and dependent on the subsolar angle. However, albedo radiation vanishes in the eclipse region of the September arc. The thermal irradiance at LRO on the nightside is 6 W/m^2 , which leads to a small total acceleration of $1 \times 10^{-9} \text{ m/s}^2$.

The accelerations of the constant and DLAM-1 albedo distributions are of very similar magnitude (in non-zero regions, rRMSE of 19 % for June and 24 % for September), although DLAM-1 exhibits irregular variations. The largest difference of $5 \times 10^{-9} \text{ m/s}^2$ occurs in the radial component for the September arc at about 0.55. Interestingly, DLAM-1 albedo radiation peaks *before* the subsolar point, where the thermal and constant albedo radiation peak. This behavior can be explained by the ground track of this orbit. Figure 13 shows the DLAM-1 albedo irradiance along the ground track over a map of the difference between DLAM-1 and the constant albedo. In this figure, the maximum albedo difference also appears before the subsolar point and coincides with a region where DLAM-1 has an albedo that is 0.067 higher or 55 % more reflective than the constant albedo of $a = 0.150$. All irregular differences between the albedo distributions seen in Figure 12 are explained by this map. However, because the thermal radiation is so much larger, the effect of these differences remains overall limited.

4.3 Change in final position

The goal of orbit determination is to estimate the state, and particularly the position, of a spacecraft over time. Therefore, the difference in position at the end of the arc between models is highly relevant. As mentioned in Section 1, the maximum allowable error is 50 m to 100 m in total position and below 1 m radially. Since the true position is not known and this paper is rather concerned with relative differences, we use a simulation without solar and lunar radiation as a baseline reference.

The differences in final positions with respect to the baseline simulation are shown in Table 4. The first number is the mean, secular difference over the final orbit (32nd revolution), and the second number gives the amplitude of periodic variations around that mean over the final orbit. Note that the periodic variation is quite large in some cases despite zero secular change.

The June arc shows a large along-track difference (more than 1 km) for the paneled target with solar radiation (A). This is likely due to accumulation of the consistently large along-track acceleration of about $-15 \times 10^{-9} \text{ m/s}^2$. However, this acceleration is of lower magnitude than the constant acceleration of $+47 \times 10^{-9} \text{ m/s}^2$ expected to result in this position difference, and of the opposite sign. For the cannonball, the along-track accelerations have a zero mean and thus the position difference is also zero. This, again, reveals how the cannonball cannot account for asymmetry; with symmetric accelerations, no secular changes occur. Interestingly, the large cross-track acceleration does not lead

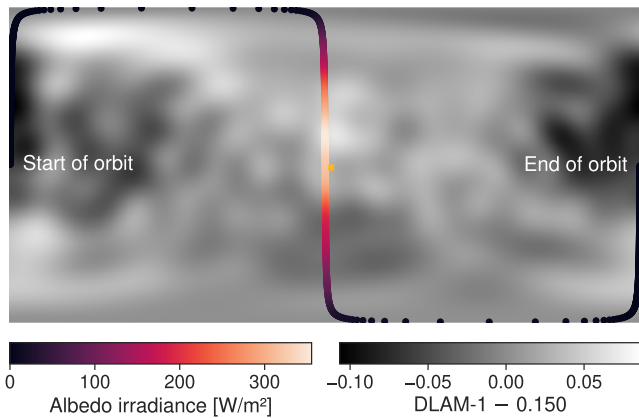


Figure 13. Ground track for September arc, colored by the irradiance due to DLAM-1 albedo. The map shows the difference between DLAM-1 and the constant albedo ($a = 0.150$). The maximum irradiance does not occur above the subsolar point (yellow star) but above the local albedo maximum 18° north of it.

solar accelerations partially. There also is an 8 m RMSE difference for the paneled model between constant and DLAM-1 albedo, the only case where the choice of albedo model influences the final position.

These differences in position emphasize the importance of RP models for precise orbit determination. The best estimate of the true effect of RP is given by setup D (solar + lunar radiation) for the paneled target. For both arcs, the maximum allowable total error would be exceeded by the sum of secular and periodic variations if RP were neglected. The radial requirement of sub-meter accuracy would be violated by periodic variations alone.

4.4 Performance

Choosing the appropriate model is not only a consideration of accuracy but also one of computational effort. The aim is to find the most efficient model that is sufficiently accurate. To determine how much less efficient complex models like paneled targets or DLAM-1 are, we measured wall time durations for different model combinations. We ran each simulation 100 times in random order on a server with 2 Intel Xeon E5-2683 v3 CPUs (14 cores, two threads per core with hyperthreading) while no other loads were present. 27 simulations ran in parallel such that all but one core were used by. More parallelism would have triggered hyperthreading, which could have skewed measurements. Tudat was compiled in release configuration with GCC 11.4.0 at optimization level $-O2$. No other steps such as CPU pinning were taken. Note that software performance can be influenced by many, seemingly innocuous aspects [54]. Still, the results show the general tendency.

The wall time durations when including solar or lunar radiation are shown in Figure 14. Again, the baseline simulation without radiation serves as a reference. The median baseline time of 4.3 min includes computations of the lunar spherical harmonics gravity model, point gravities from Sun and Earth, and general integration and propagation. Solar radiation has a negligible complexity, even for a paneled target. Lunar radiation with constant albedo increases the duration by about 20 %, but slightly more for the paneled than the cannonball target. Taking the albedo from the

spherical harmonics expansion of DLAM-1 increases the duration by up to 80 % compared to the baseline. This is a significant performance penalty, which may not always be tolerable. Other authors even report increases of several hundred percent for DLAM-1 albedo [10].

The durations are relatively consistent as indicated by the inter-quartile range of at most 5 s. Still, all distributions have a long tail toward longer durations: the difference between maximum and median is between 9 and 21 times higher than the difference between minimum and median. This skewness is typical for software performance.

5 Conclusion

We described a collection of RP models of varying levels of complexity, then examined the differences in short-term orbital effects of RP on LRO between these models. There are large seasonal differences in the RP accelerations: for small β (e.g., around September), the accelerations are mainly radial and along-track, while they are predominantly cross-track for $\beta \approx \pm 90^\circ$ (e.g., around June). After 2.5 days, the position diverged from the no-RP baseline by up to 1100 m in June and 80 m in September. Periodic variations of up to 50 m are superimposed over the orbit on the secular differences. In September, the periodic variations are damped by lunar accelerations that oppose solar accelerations. Large differences also exist between the representations of LRO as a cannonball and a paneled target: due to the cannonball's symmetry, accelerations do not cancel over an orbit and are generally smaller than those of a paneled target, which can have the solar array track the Sun. Thermal radiation dominates the lunar emissions, and a constant albedo distribution is both sufficiently accurate and computationally cheaper than the spherical harmonics expansion DLAM-1.

Our results showed that RP is essential for precise orbit determination of the LRO. Both the total and radial accuracy requirements would be violated otherwise. However, not all models are worth the computational effort. We recommend the following setup:

- Solar radiation should be included since it is significant yet computationally cheap.

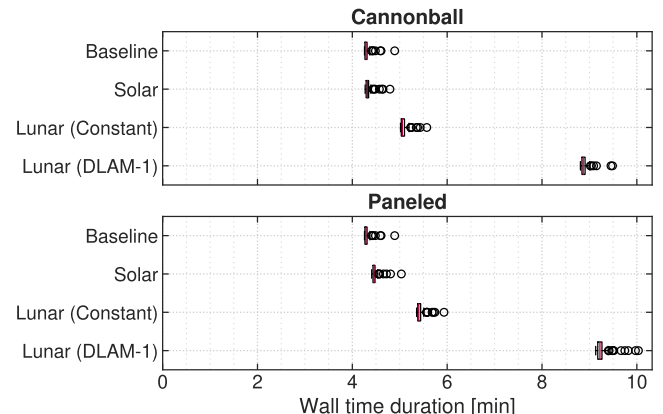


Figure 14. Wall time duration of simulations with different RP models. The statistics come from 100 runs for each model. Evaluation of DLAM-1's spherical harmonics expansion increases the duration by up to 80 %.

40. A. McEwen and M. Robinson, “Mapping of the Moon by Clementine,” *Advances in Space Research*, vol. 19, no. 10, pp. 1523–1533, Jan. 1997. DOI: [10.1016/s0273-1177\(97\)00365-7](https://doi.org/10.1016/s0273-1177(97)00365-7).
41. M. Iqbal, *Introduction to Solar Radiation*. Academic Press Canada, 1983.
42. Y. Shkuratov, V. Kaydash, V. Korokhin, Y. Velikovsky, N. Opanasenko, and G. Videen, “Optical measurements of the Moon as a tool to study its surface,” *Planetary and Space Science*, vol. 59, no. 13, pp. 1326–1371, Oct. 2011. DOI: [10.1016/j.pss.2011.06.011](https://doi.org/10.1016/j.pss.2011.06.011).
43. B. J. Buratti, J. K. Hillier, and M. Wang, “The Lunar Opposition Surge: Observations by Clementine,” *Icarus*, vol. 124, no. 2, pp. 490–499, Dec. 1996. DOI: [10.1006/icar.1996.0225](https://doi.org/10.1006/icar.1996.0225).
44. B. Hapke, *Theory of reflectance and emittance spectroscopy*. Cambridge University Press, 2012.
45. R. S. Park *et al.*, “Estimating a High-Resolution Lunar Gravity Field and Time-Varying Core Signature,” in *AGU Fall Meeting Abstracts*, vol. 2011, Dec. 2011, P44B-06, P44B-06.
46. J. L. Bandfield, P. O. Hayne, J.-P. Williams, B. T. Greenhagen, and D. A. Paige, “Lunar surface roughness derived from LRO Diviner Radiometer observations,” *Icarus*, vol. 248, pp. 357–372, Mar. 2015. DOI: [10.1016/j.icarus.2014.11.009](https://doi.org/10.1016/j.icarus.2014.11.009).
47. NASA Science Mission Directorate. “Spacecraft Icons.” (2018), [Online]. Available: <https://science.nasa.gov/get-involved/toolkits/spacecraft-icons>.
48. M. Mesarch, M. Beckman, D. Folta, R. Lamb, and K. Richon, “Maneuver Operations Results from the Lunar Reconnaissance Orbiter (LRO) Mission,” in *SpaceOps 2010 Conference*, American Institute of Aeronautics and Astronautics, Apr. 2010. DOI: [10.2514/6.2010-1985](https://doi.org/10.2514/6.2010-1985).
49. A. Löcher and J. Kusche, “Precise orbits of the Lunar Reconnaissance Orbiter from radiometric tracking data,” *Journal of Geodesy*, vol. 92, no. 9, pp. 989–1001, Feb. 2018. DOI: [10.1007/s00190-018-1124-4](https://doi.org/10.1007/s00190-018-1124-4).
50. W. M. Folkner, J. G. Williams, and D. H. Boggs, “The planetary and lunar ephemeris DE 421,” *IPN progress report*, vol. 42, no. 178, p. 1, 2009.
51. B. A. Archinal *et al.*, “Report of the IAU Working Group on Cartographic Coordinates and Rotational Elements: 2009,” *Celestial Mechanics and Dynamical Astronomy*, vol. 109, no. 2, pp. 101–135, Dec. 2010. DOI: [10.1007/s10569-010-9320-4](https://doi.org/10.1007/s10569-010-9320-4).
52. Goddard Space Flight Center, “A Standardized Lunar Coordinate System for the Lunar Reconnaissance Orbiter and Lunar Datasets, LRO Project and LGCWG White Paper,” Tech. Rep., Oct. 1, 2008.
53. S. Goossens, Á. F. Mora, E. Heijkoop, and T. J. Sabaka, “Patched Local Lunar Gravity Solutions Using GRAIL Data,” *Earth and Space Science*, vol. 8, no. 11, Oct. 2021. DOI: [10.1029/2021ea001695](https://doi.org/10.1029/2021ea001695).
54. T. Mytkowicz, A. Diwan, M. Hauswirth, and P. F. Sweeney, “Producing wrong data without doing anything obviously wrong!” *ACM SIGPLAN Notices*, vol. 44, no. 3, pp. 265–276, Feb. 2009. DOI: [10.1145/1508284.1508275](https://doi.org/10.1145/1508284.1508275).